

DAMAGE MODELLING WITH SMOOTHED POINT INTERPOLATION METHODS

Lapo Gori

Samuel Silva Penna

Roque Luiz da Silva Pitangueira

lapo@dees.ufmg.br

spenna@dees.ufmg.br

roque@dees.ufmg.br

*Structural Engineering Department, Engineering School, Federal University of Minas Gerais
Avenida Antônio Carlos, 6627, 31270901, Belo Horizonte, MG, Brazil*

Abstract. Due to the non-local character embedded in their formulation, meshfree methods belonging to the class of Smoothed Point Interpolation Methods (S-PIMs) have been recently shown to possess certain regularization properties when applied to localization problems. Since meshfree methods usually provide only a weak regularization effect, the combination with other regularization strategies is often necessary. The present work aims to exploit the regularization properties of S-PIMs strategies in the analysis of quasi-brittle media with scalar damage models; a stronger regularization effect is obtained combining the meshfree approach with the micropolar continuum theory, another well-known regularization strategy. The basic theoretical and computational aspects of the application of two S-PIM strategies, the Edge-Based Smoothed Point Interpolation Method (ES-PIM) and Node-Based Smoothed Point Interpolation Method (NS-PIM), to micropolar damage models are discussed, and numerical simulations of two plain concrete experimental tests are presented.

Keywords: Smoothed Point Interpolation Methods (SPIMs), Meshfree methods, Strain localization, Continuum damage mechanics, Micropolar theory

1 Introduction

The analysis of strain-softening problems with the standard finite element method (FEM) has always been a challenging task, due to the presence of a number of pathological behaviours such as *strong mesh-dependency*, *premature fracture initiation*, and *instantaneous perfectly-brittle fracture* [1, 2]. These pathological effects are associated to the so-called *strain localization* phenomenon. It is known that these pathological behaviours are due to the *local* representation offered by the classic continuum theory, in contrast with the *non-local* nature of phenomena like damage and plasticity [3]. The main aim of the strategies proposed in the literature to solve this problem (the so-called regularization techniques) is the introduction of an *internal length*, allowing to recover the non-local character of the phenomenon. Two approaches have been proposed in the past. The first one consists in the introduction of an internal length directly in the continuum model (i.e., at the *formulation level*); an interesting overview on the different regularization methods can be found in the papers by de Borst et al. [1] and by Bažant et al. [4]. Among the different alternatives there are: *non-local* and *gradient-enhanced* models [2, 5–10], *viscous* models [11], *cohesive zone* models [12, 13], methods based on the *fracture energy approach* [14], *phase-field* models [15–17], and the *micropolar* theory [18–26]. The other approach consists in the introduction of the internal length at the *numerical level*. Among the various solutions based on the finite element method there are, for example, the use of elements with embedded discontinuities [27], able to represent various kind of weak and strong discontinuities, or elements with embedded localization zones [28, 29]. It has been also shown that some classes of *meshfree* methods, like *moving least square* (MLS) and *reproducing kernel* (RK) approximations, as well as methods based on *strain smoothing* techniques, are able to bring regularization effects on localization problems [30–37], due to their intrinsic *non-local* properties. Recently, the regularization effects of the meshfree methods belonging to the class of *smoothing point interpolation methods* (S-PIMs) [38–41] have been investigated for the case of scalar damage by Gori et al. [37]. Aiming to combine the regularization properties of such methods with the ones induced by the micropolar continuum theory, the same authors also recently proposed an extension of the SPIM approach to this continuum theory [42].

Taking into account the results provided in the papers by Gori et al. [37, 42], this paper aims to present some numerical results obtained with the combination of the micropolar continuum theory (a regularization strategy at the formulation level) with some of the meshfree methods belonging to the class of smoothed point interpolation methods (regularization strategies at the numerical level), for the analysis of problems described with scalar damage models. The first part of the paper provides the basic concepts on the micropolar formulation, both for linear elasticity and scalar damage. Then, some basic details regarding the use of SPIMs strategies with the micropolar formulation are provided. Finally, two simulations of plain concrete experimental tests are provided, in order to point out the qualities of the aforementioned combination. The numerical implementations of the strategies discussed in this paper, as well as the numerical simulations, have been performed in the open-source software **INSANE**¹. The triangular background cells used for the construction of the meshfree discretizations have been generated with the software **Gmsh** [43].

2 Micropolar media

In a geometrically-linear context, the configuration of a micropolar continuum is characterized by a *displacement field* \bar{u} and a *microrotation field* $\bar{\varphi}$, leading to the strain measures

$$\underline{\gamma} = \text{grad}^T(\bar{u}) - \mathbf{e} \cdot \bar{\varphi} = (u_{j,i} - \mathbf{e}_{ijk} \varphi_k) \bar{e}_i \otimes \bar{e}_j \quad (1)$$

$$\underline{\kappa} = \text{grad}^T(\bar{\varphi}) = \varphi_{j,i} \bar{e}_i \otimes \bar{e}_j \quad (2)$$

which are referred to as *strain tensor* and *micro-curvature tensor*, respectively, and where the symbol \mathbf{e} indicates the standard *Levi-Civita* operator with three indexes. To these strain measures correspond,

¹ More informations on the project can be found at <https://www.insane.dees.ufmg.br/>; the development code is freely available at the Git repository <http://git.insane.dees.ufmg.br/insane/insane.git>.

respectively, the *stress tensor* $\underline{\sigma}$ and the *couple-stress tensor* $\underline{\mu}$, which, in a quasi-static context, must satisfy the local equilibrium equations for forces and moments

$$\operatorname{div}^T(\underline{\sigma}) + \bar{b}_V = \bar{0} \longrightarrow \sigma_{ij,i} + b_{Vj} = 0 \quad (3)$$

$$\operatorname{div}^T(\underline{\mu}) + \mathbf{e} \cdot \underline{\sigma} + \bar{l}_V = \bar{0} \longrightarrow \mu_{ij,i} + \mathbf{e}_{jkl} \sigma_{kl} + l_{Vj} = 0 \quad (4)$$

where \bar{b}_V and \bar{l}_V represent, respectively, volume forces and volume couples acting in the body domain.

In the case of linear elasticity and disregarding the direct coupling between the Cauchy-type and Cosserat-type effects (i.e., the *chirality* effect) stress and deformation measures are linked by the following constitutive equations

$$\underline{\sigma} = \hat{\mathbf{A}} : \underline{\gamma} \quad (5)$$

$$\underline{\mu} = \hat{\mathbf{C}} : \underline{\kappa} \quad (6)$$

The expressions above can be recasted in the following compact form [25, 44], in terms of the *generalized stress* ($\underline{\Sigma}$), *strain* ($\underline{\Gamma}$) and constitutive ($\hat{\mathcal{E}}$) operators

$$\underline{\Sigma} = \hat{\mathcal{E}} : \underline{\Gamma} \rightarrow \begin{pmatrix} \underline{\sigma} & \underline{0} \\ \underline{0} & \underline{\mu} \end{pmatrix} = \hat{\mathcal{E}} : \begin{pmatrix} \underline{\gamma} & \underline{0} \\ \underline{0} & \underline{\kappa} \end{pmatrix} \quad (7)$$

Assuming an initially *isotropic* material in a plane-stress state, the generalized constitutive expression reduces to the following matricial expression

$$\{\underline{\Sigma}\} = [\hat{\mathcal{E}}] \{\underline{\Gamma}\} \longrightarrow \begin{pmatrix} \sigma_{xx} \\ \sigma_{xy} \\ \sigma_{yx} \\ \sigma_{yy} \\ \mu_{xz} \\ \mu_{yz} \end{pmatrix} = \begin{pmatrix} \frac{E}{1-\nu^2} & 0 & 0 & \frac{\nu E}{1-\nu^2} & 0 & 0 \\ 0 & G + G_c & G - G_c & 0 & 0 & 0 \\ 0 & G - G_c & G + G_c & 0 & 0 & 0 \\ \frac{\nu E}{1-\nu^2} & 0 & 0 & \frac{E}{1-\nu^2} & 0 & 0 \\ 0 & 0 & 0 & 0 & 2GL_b^2 & 0 \\ 0 & 0 & 0 & 0 & 0 & 2GL_b^2 \end{pmatrix} \begin{pmatrix} \gamma_{xx} \\ \gamma_{xy} \\ \gamma_{yx} \\ \gamma_{yy} \\ \kappa_{xz} \\ \kappa_{yz} \end{pmatrix} \quad (8)$$

where E , G , and ν are the classic Young's modulus, shear modulus, and Poisson's ratio, while G_c and L_b are additional material parameters [18], the Cosserat's shear modulus and internal bending length, respectively.

2.1 Scalar damage

The extension to scalar damage is straightforward [24–26], resulting in the following secant and incremental stress-strain relations

$$\underline{\Sigma} = \hat{\mathcal{E}}^S : \underline{\Gamma}, \quad \hat{\mathcal{E}}^S = (1 - D) \hat{\mathcal{E}} \quad (9)$$

$$\dot{\underline{\Sigma}} = \hat{\mathcal{E}}^t : \dot{\underline{\Gamma}}, \quad \hat{\mathcal{E}}^t = (1 - D) \hat{\mathcal{E}} - \frac{\partial D(\Gamma_{eq})}{\partial \Gamma_{eq}} \left(\underline{\Sigma}^0 \otimes \frac{\partial \Gamma_{eq}}{\partial \underline{\Gamma}} \right), \quad \underline{\Sigma}^0 := \hat{\mathcal{E}} : \underline{\Gamma} \quad (10)$$

where D is the scalar damage variable, assumed to vary from 0 (undamaged material) to 1 (completely damaged material) according to a prescribed evolution law $D(\Gamma_{eq})$. In the numerical simulations of section 4, the following exponential damage law is considered

$$D(\Gamma_{eq}) = 1 - \frac{K_0}{\Gamma_{eq}} \left(1 - \alpha + \alpha e^{-\beta(\Gamma_{eq} - K_0)} \right) \quad (11)$$

where K_0 is a threshold value for the equivalent deformation Γ_{eq} , representing the onset of damage, and where α and β are parameters that define, respectively, the maximum allowed damage level and the damage evolution intensity. Different scalar damage models can be obtained choosing a peculiar equivalent deformation; the one adopted in the examples of section 4 is an extension to the micropolar formulation of the classic Mazars [25, 45, 46] model, defined by the equivalent deformation

$$\Gamma_{eq} = \sqrt{\left[\sum_{k=1}^3 \langle \varepsilon^{(k)} \rangle_+ \right]^2} \quad (12)$$

where $\varepsilon^{(k)}$ the k-th eigenvalue of the symmetric part of the strain tensor $\underline{\gamma}$, and $\langle \varepsilon^{(k)} \rangle_+ = (\varepsilon^{(k)} + |\varepsilon^{(k)}|)/2$ its positive part.

3 Micropolar smoothed point interpolation methods

In S-PIM strategies for micropolar media the field variables of the coupled boundary value problem, i.e., the displacement field $\bar{u}(p)$ and microrotation field $\bar{\varphi}(p)$ at each point $p \in \mathbf{D}$, where \mathbf{D} is the domain of the problem, are approximated by the functions $\bar{u}^h(p)$ and $\bar{\varphi}^h(p)$ (organized in a certain array $\{U(p)\}$) as [42]

$$\{U(p)\} = \sum_{i \in S_d} [\phi_i(p)] \{d_i\} = \sum_{i \in S_d} \begin{pmatrix} [\phi_{Ai}(p)] & [0] \\ [0] & [\phi_{Ci}(p)] \end{pmatrix} \begin{pmatrix} \{d_{Ai}\} \\ \{d_{Ci}\} \end{pmatrix} \quad (13)$$

where the index i indicates a node p_i in the *support domain* S_d , i.e., the set of nodes in the neighbourhood of the point $p \in \mathbf{D}$, $[\phi_i(p)]$ is the nodal matrix of approximation functions, and $\{d_i\}$ is an array containing the nodal parameters of the field variables at the node i . The subscripts A and C are used to distinguish between Cauchy-like and Cosserat-like terms

$$\bar{u}^h(p) = \sum_{i \in S_d} [\phi_{Ai}(p)] \{d_{Ai}\}, \quad \bar{\varphi}^h(p) = \sum_{i \in S_d} [\phi_{Ci}(p)] \{d_{Ci}\} \quad (14)$$

The shape functions, in this class of methods, are usually generated using the *point interpolation method* (PIM) [47], or the *radial PIM* (RPIM) *with polynomial reproduction* [48], and are characterized by the following properties: they are linearly independent, possess the Kronecker delta property, form a partition of unity, possess the linear reproducing property, present compact support, and are *not compatible*. The lack of compatibility, consisting in the possibility of having discontinuities in the approximated fields, results in functions that don't belong to the Hilbert space $\mathcal{H}^1(\mathbf{D})$ of square-integrable functions with square-integrable first derivative. Liu [39, 40] showed that such functions belong to a different *discretized* Hilbert space $\mathcal{G}_h^1(\mathbf{D})$, which he called *G-space*, of functions that don't possess a square-integrable first derivative. A micropolar G-space was proposed by Gori et al. [42].

In order to allow the use of non-compatible interpolation functions, it is necessary to introduce *smoothed derivatives* when calculating the measures of deformations of Eqs. (1) and (2). The first step consists in the discretization of the problem domain into a set of N_S non-overlapping *smoothing domains* \mathbf{D}_k^S , with $k = 1, \dots, N_S$. Two common strategies are constituted by the *node-based smoothed point interpolation method* (NS-PIM) [49–51] and the *edge-based smoothed point interpolation method* (ES-PIM) [52], represented in Fig. 1(a) and 1(b), respectively. Both these methods are based on a set of non-overlapping *background cells* which, in plane problems, are usually triangular. Then, at each point $p \in \mathbf{D}_k^S$, the strain measures of Eq. 1 and 2 are replaced by *smoothed strain measures*, constant over the smoothing domain \mathbf{D}_k^S , and expressed by [42]

$$\underline{\tilde{\gamma}}(U(p_k)) = \frac{1}{A_k} \int_{\partial \mathbf{D}_k^S} \bar{n}^{(k)}(\xi) \otimes \bar{u}(\xi) \, dS - \mathbf{e} \cdot \bar{\varphi}(U(p_k)) \quad (15)$$

$$\underline{\tilde{\kappa}}(U(p_k)) = \frac{1}{A_k} \int_{\partial \mathbf{D}_k^S} \bar{n}^{(k)}(\xi) \otimes \bar{\varphi}(\xi) \, dS \quad (16)$$

where $A_k = \int_{\mathbf{D}_k^S} d\mathcal{V}$, and $\bar{n}^{(k)}$ is the unitary outward normal vector field on the boundary $\partial\mathbf{D}_k^S$. Further details on the theoretical aspects of SPIMs strategies applied to damage mechanics and to micropolar media can be found in the papers by Gori et al. [37, 42].

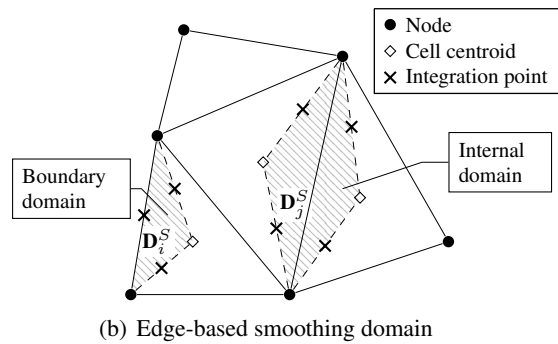
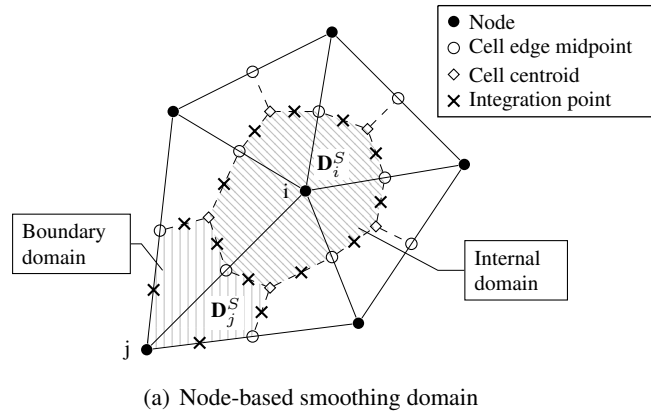


Figure 1. Smoothing domains

4 Numerical simulations

The present section illustrates the numerical simulations of two different plain concrete experimental tests, performed using the resources discussed in sections 2 and 3. The first one (section 4.1) is the L-shaped panel investigated experimentally by Winkler et al. [53], while the second one (section 4.2) is the four points shear test by Arrea and Ingraffea [54]; both of them has been widely used in the literature as benchmark tests for numerical investigations on concrete behaviour [55–64]. These examples has been selected to point out the mesh objectivity properties of the SPIMs, both alone and in combination with the micropolar continuum theory. In order to illustrate the capability of the adopted strategies to reproduce the general behaviour of the selected experimental test, the experimental results has been presented together with the equilibrium path of the simulations. It is remarked, however, that the aim was not to exactly reproduce the experimental results, since this would have required accurate calibrations of the damage laws and, possibly, the use of damage models more complex than a simple scalar one, able to better capture the physical behaviour of the samples.

4.1 L-shaped panel

The plain concrete L-shaped panel depicted in Fig. 2 was characterized by a Young's modulus $E = 25850 \text{ N/mm}^2$, a Poisson's ratio $\nu = 0.18$, tensile and compressive uniaxial strengths $f_t = 2.7 \text{ N/mm}^2$ and 4.0 N/mm^2 , a fracture energy $G_f = 0.065 \text{ N/mm}^2$, and a characteristic length of the material $h = 28 \text{ mm}$; in the following simulations its behaviour was reproduced adopting the *Mazars* scalar damage model (Eq. (12)), with the following parameters for the exponential damage law, $\alpha = 0.950$, $\beta = 1100$ and $K_0 = 1.12 \times 10^{-4}$.

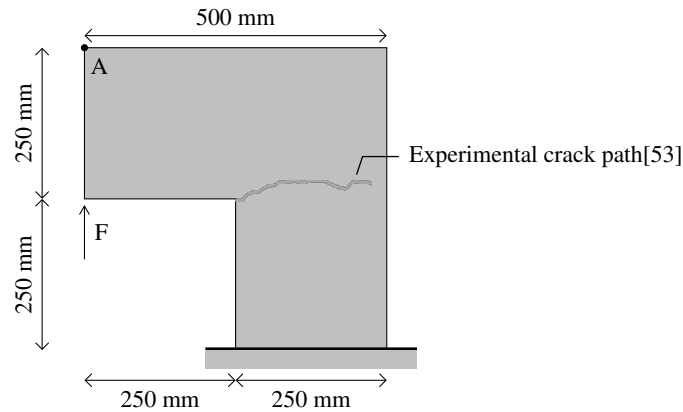


Figure 2. L-shaped panel geometry

The sample of Fig. 2 was first investigated with the FEM, using four different discretizations (Fig. 3), each one composed by three-node triangular elements in a plane-stress state, with a thickness of 100 mm. The four meshes were characterized by a different mean nodal spacing near the concave corner, equal to 25 mm, 15 mm, 10 mm, and 5 mm, while it was equal to 50 mm elsewhere. The sample was also investigated with the NS-RPIM and ES-RPIM, using the discretizations of Figs. 4 and 5; it should be noted that the node- and edge-based discretizations were constructed using the triangular finite elements illustrated in Fig. 3 as background cells, maintaining the same nodal distributions adopted in the FEM simulations. At each integration point of the node- and edge-based discretizations, the support domains were constructed using the T-schemes T3 and T6/3 [38], as well as the influence domain strategy usually adopted in the *Element-Free Galerkin* (EFG) method. The meshfree shape functions were constructed with the radial point interpolation method with polynomial reproduction, using the exponential radial function with $c = 0.002$, and adopting 3 polynomial terms. The analyses were performed adopting a loading process driven by the *generalized displacement control method* [65], assuming a reference load $F = 7000$ N, an initial loading factor increment of 0.005, and a tolerance for convergence in relative displacement of 1×10^{-4} . All the simulations presented in this section were performed considering the tangent approximation of the constitutive operator, except for some of the meshfree simulations with influence domains, which required a secant approximation due to convergence issues.

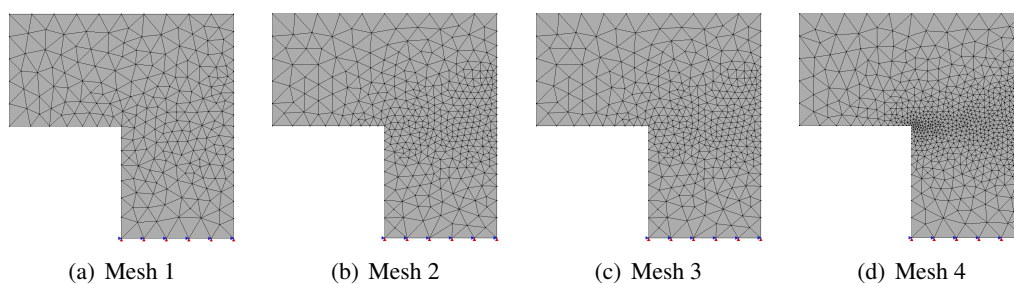


Figure 3. L-shaped panel FEM meshes

The results of the FEM analyses are illustrated in Fig. 6, where the values of the vertical displacement at the point A of Fig. 2 are plotted against the load factor, together with the experimental range presented by Winkler et al.[53]. As expected, due to the strain-softening behaviour of the adopted model, the results were strongly mesh-dependent, with the finer meshes presenting peak values of the load factor sensibly lower with respect to the coarsest meshes.

As it can be observed from Fig. 7 also the meshfree simulations with the T-schemes presented a certain dependence of the results on the discretization, though with equilibrium paths less dispersed with respect to the ones of the FEM simulations. Comparing the different meshfree strategies it can be observed that the equilibrium paths produced with the ES-RPIM T6/3 were the ones with the minor dis-

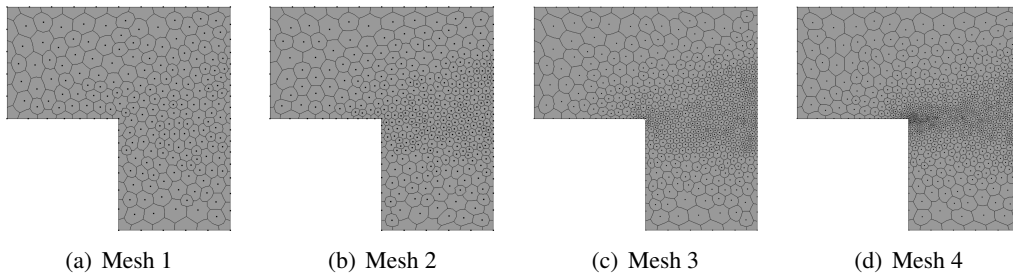


Figure 4. L-shaped panel node-based discretizations

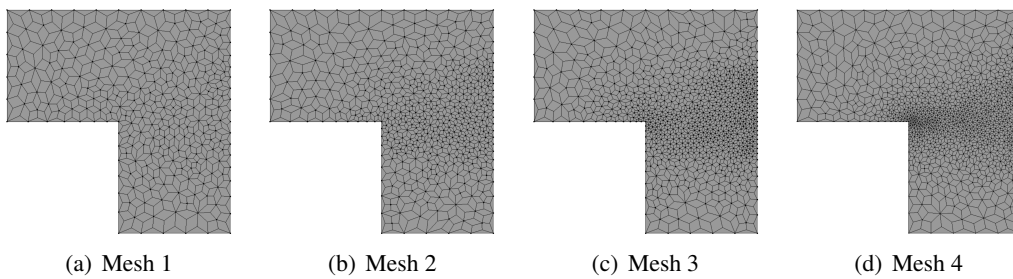


Figure 5. L-shaped panel edge-based discretizations

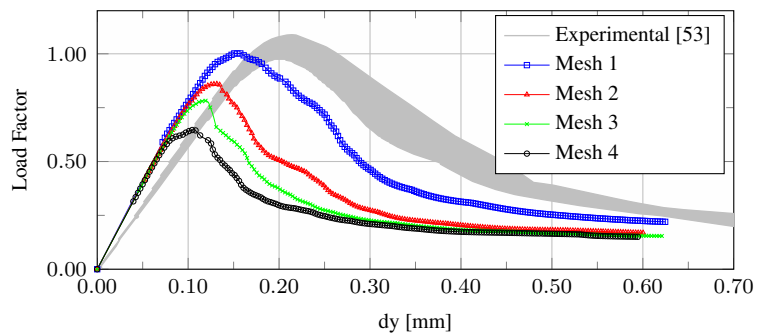


Figure 6. L-shaped panel - FEM equilibrium paths

persion; since the T6/3 scheme considers a larger number of support nodes with respect to the T3 scheme at each integration point, this points out the benefits associated with degree of nonlocality embedded in their formulation.

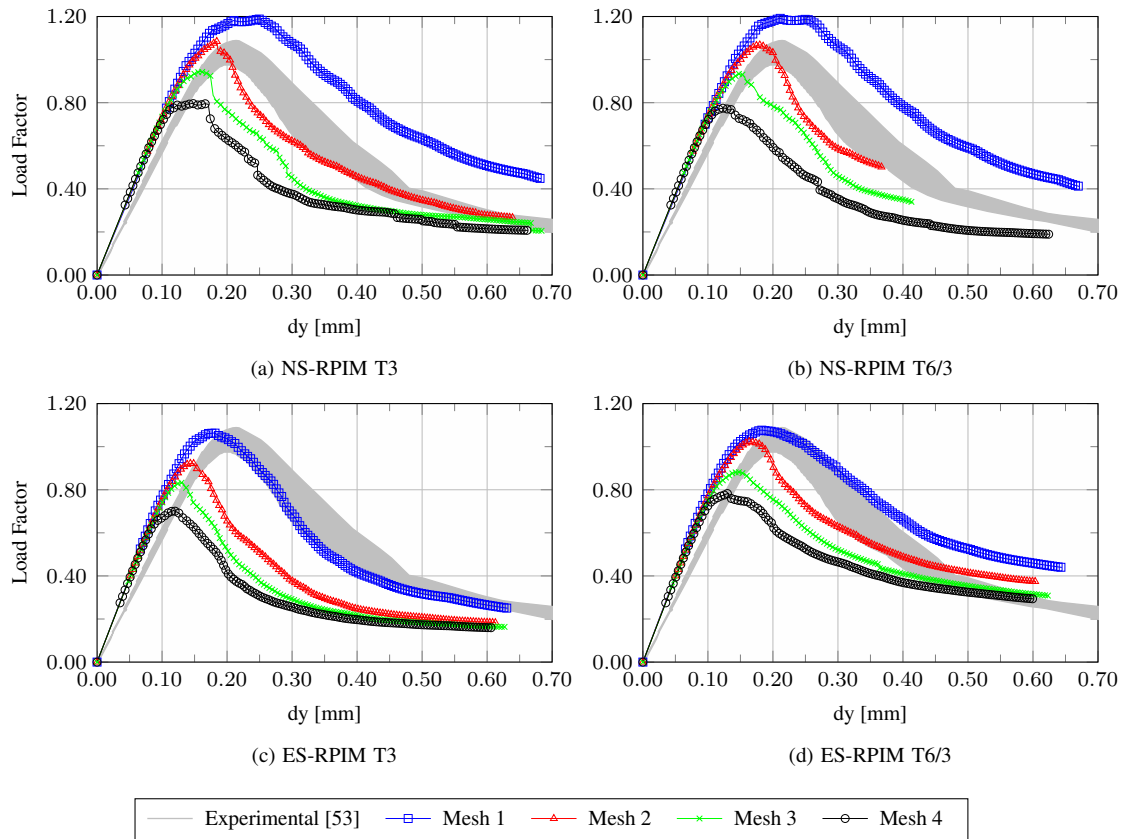


Figure 7. L-shaped panel - SPIMs equilibrium paths

In order to better exploit the advantages of the nonlocal character of the SPIMs strategies, the simulations of with the edge-based approach were repeated using influence domains for the support nodes selection. While the the spatial size of the support domains produced with the T-schemes is dependent on the discretization, if the support nodes are selected using the influence domains strategy it is possible to obtain support domains with a spatial size that is independent of the discretization refinement. In order to obtain the results depicted in Fig. 8, the support nodes of the edge-based discretizations were selected using circular influence domains in the region near the concave corner, with radii equal to 20, 25 and 30 mm. As it can be observed in Fig. 8, when circular influence domains with radius $R = 20$ mm were adopted, the meshes 3 and 4 exhibited almost the same equilibrium path, with a slight discrepancy in the softening branch. For the values $R = 25$ mm and $R = 30$ mm the two discretizations still manifested the same peak value, though with larger differences in the post-peak branch. Furthermore, it should be noted that to higher radii corresponded higher peak values. Considering the results obtained for the mesh 2, it is interesting to observe that as the radius of the influence domains was increased, the difference in terms of peak-values between the mesh 2 and the meshes 3 and 4 tended to decrease, emphasizing the behaviour obtained with the T6/3 scheme.

4.2 Four-points shear test

The mixed-mode fracture test depicted in Fig. 9 was characterized by a Young's modulus $E = 24800$ N/mm², Poisson's ratio $\nu = 0.20$, tensile uniaxial strength between 2.8 N/mm² and 4.0 N/mm², and fracture energy between 0.10 N/mm² and 0.14 N/mm²; in the following simulations its behaviour was reproduced adopting the *Mazars* scalar damage model (Eq. (12)), with the following parameters for the exponential damage law, $\alpha = 0.950$, $\beta = 1000$ and $K_0 = 1.6 \times 10^{-4}$. The additional micropolar elastic

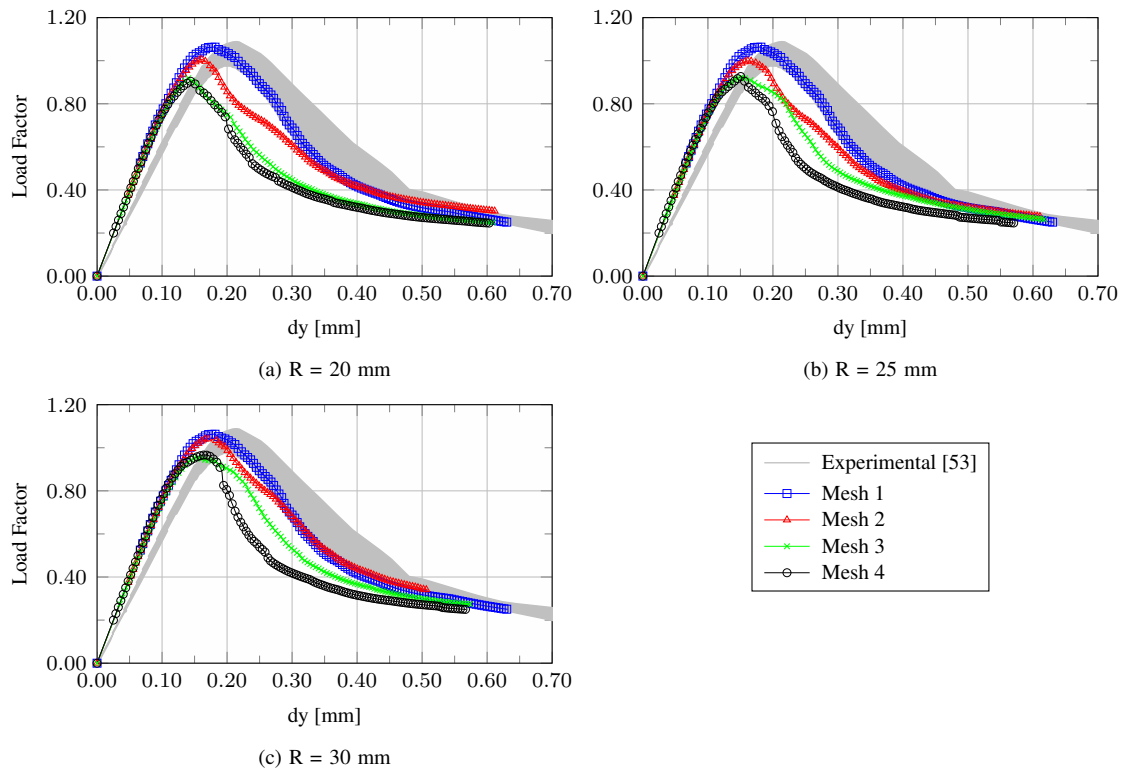


Figure 8. L-shaped panel - ES-RPIM with influence domains strategy - Equilibrium paths

parameters were a Cosserat's shear modulus $G_c = 3500 \text{ N/mm}^2$, and two different values of the internal bending length L_b , equal to 5.0 and 10.0 mm.

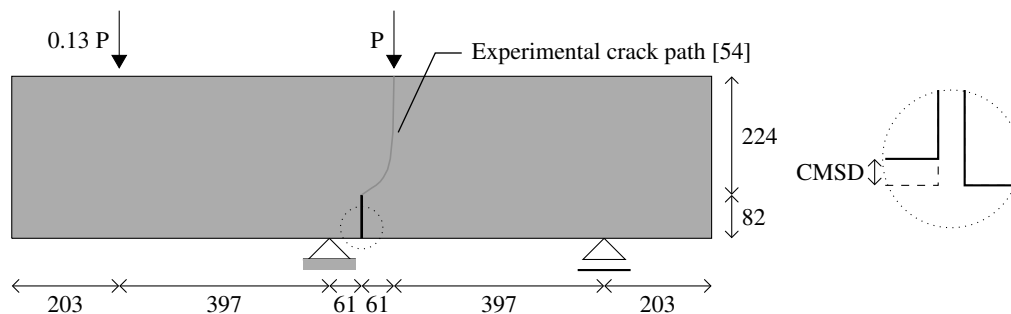


Figure 9. Four-point shear test - Geometry (measures in mm)

The sample of Fig. 9 was first investigated with the FEM, using three different discretizations (Fig. 10), each one composed by three-node triangular elements in a plane-stress state, with a thickness of 156 mm. The three meshes were characterized by a mean nodal spacing of 30 mm, 20 mm, and 10 mm between the notch and the point of application of the load P , and 70 mm elsewhere. The notch was represented as sharp, with an initial opening of 5 mm at its base. The sample was also investigated with the ES-RPIM, using the discretizations of Fig. 11, based on the same nodal distributions adopted in the FEM simulations. At each integration point of the node- and edge-based discretizations, the support domains were constructed using the T-schemes T3 and T6/3 [38]. The meshfree shape functions were constructed with the radial point interpolation method with polynomial reproduction, using the exponential radial function with $c = 0.002$, and adopting 3 polynomial terms. The analyses were performed adopting a loading process driven by the *generalized displacement control method* [65], assuming a reference load $P = 130000 \text{ N}$, an initial loading factor increment of 0.0125, and a tolerance for convergence in relative displacement of 1×10^{-4} . All the simulations presented in this section were performed considering the

tangent approximation of the constitutive operator.

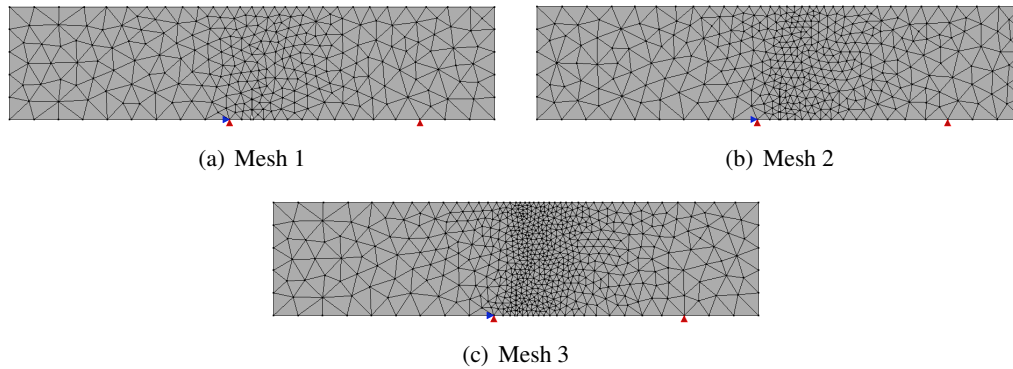


Figure 10. Four-point shear test - FEM meshes

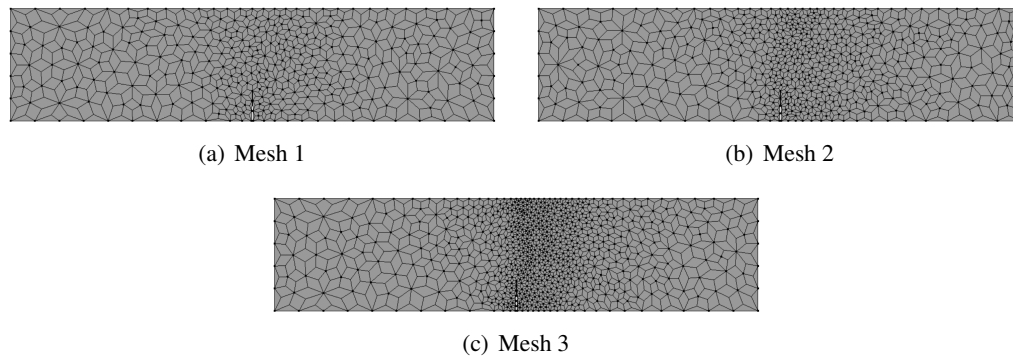


Figure 11. Four-point shear test - ES-RPIM meshes

The results of the FEM analyses are illustrated in Fig. 12, in terms of the *crack mouth sliding displacement* (CMSD) plotted against the load factor, together with the experimental results obtained by Arrea and Ingraffea [54]. As in the case of the L-panel presented in section 4.1, it can be observed that the FEM results were strongly mesh-dependent, with the finer meshes presenting peak values of the load factor sensibly lower with respect to the coarsest meshes. As for the L-panel of the previous section, also for the four point shear test investigated here the ES-RPIM strategy provided less dispersed results if compared with the FEM, especially when the T6/3 support nodes selection scheme was adopted.

5 Conclusions

The main aim of this paper was to illustrate some numerical results regarding the combination of the micropolar continuum theory with meshfree methods belonging to the class of smoothed point interpolation methods for the analysis of problems described in terms of scalar damage models. For this purpose, two plain concrete experimental tests were selected. The results that were obtained clearly show some advantages with respect to simulations performed with the standard FEM. As pointed out by the equilibrium paths presented in section 4, while the FEM simulations presented a strong mesh dependency, the ones performed with the meshfree approach and the micropolar theory exhibited less dispersed results, especially when spatially larger support domains were adopted. These results point out the effectiveness of the proposed approach as a regularization strategy for strain localization problems, and justify further investigations to exploit this strategy.

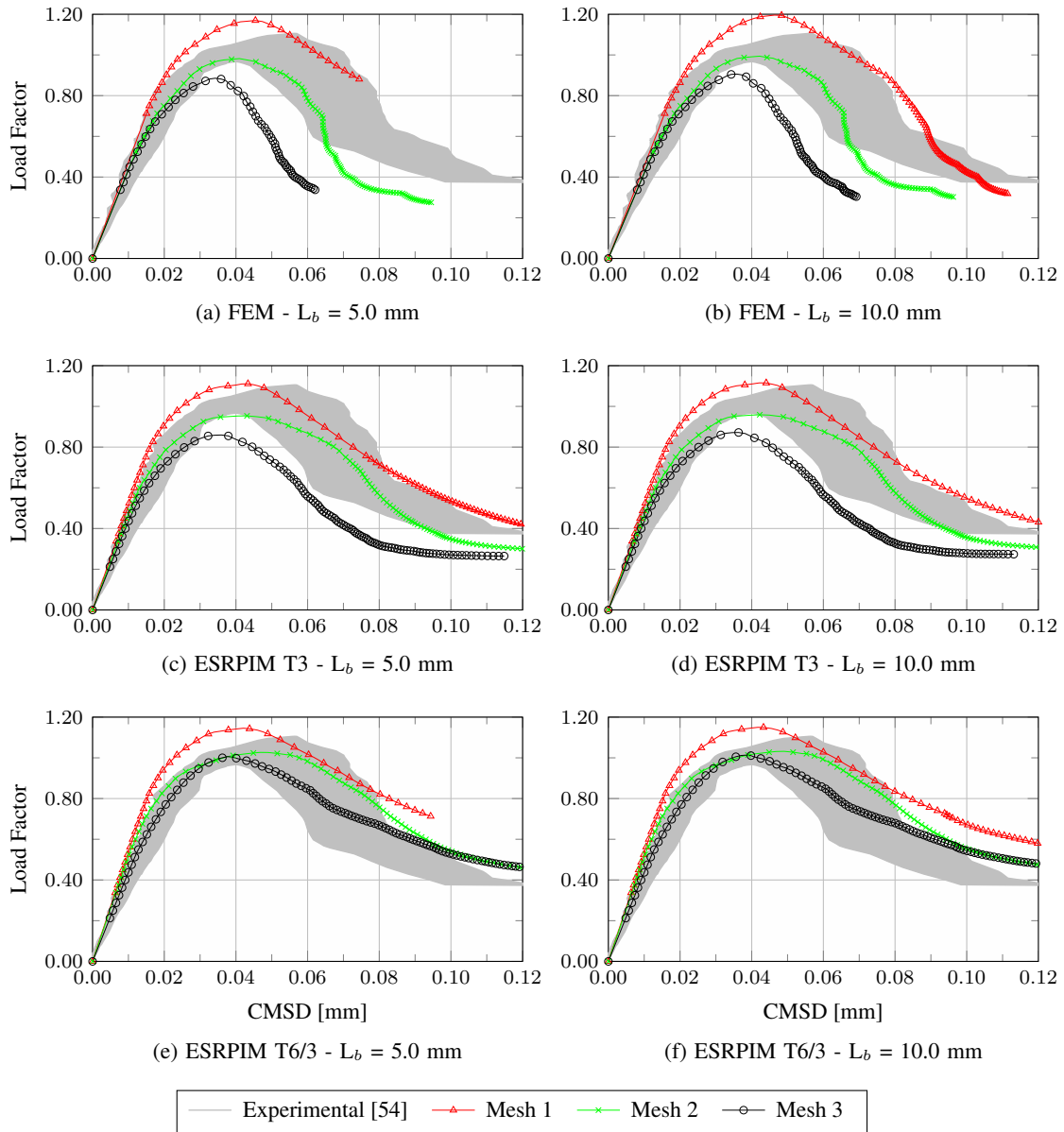


Figure 12. Four-point shear test equilibrium paths

Acknowledgements

The authors gratefully acknowledge the support of the brazilian research agencies CAPES (in portuguese: *Coordenação de Aperfeiçoamento de Pessoal de Nível Superior*), FAPEMIG (in portuguese: *Fundação de Amparo à Pesquisa do Estado de Minas Gerais*) and CNPq (in portuguese: *Conselho Nacional de Desenvolvimento Científico e Tecnológico* - grant 309515/2017-3).

References

- [1] de Borst, R., Sluys, L., Mühlhaus, H.-B., & Pamin, J., 1993. Fundamental issues in finite element analyses of localization of deformation. *Engineering Computations*, vol. 10, pp. 99–121.
- [2] Peerlings, R., de Borst, R., Brekelmans, W., & Geers, M., 2002. Localisation issues in local and nonlocal continuum approaches to fracture. *European Journal of Mechanics, A/Solids*, vol. 21, pp. 175–189.
- [3] Bažant, Z., 1991. Why continuum damage is nonlocal: micromechanics arguments. *Journal of Engineering Mechanics*, vol. 117, n. 5, pp. 1070–1087.
- [4] Bažant, Z. & Jirásek, M., 2002. Nonlocal integral formulations of plasticity and damage: survey of progress. *Journal of Engineering Mechanics*, vol. 128, n. 11, pp. 1119–1149.
- [5] Bažant, Z. & Lin, F.-B., 1988. Non-local yield limit degradation. *International Journal for Numerical Methods in Engineering*, vol. 26, n. 8, pp. 1805–1823.
- [6] Pijaudier-Cabot, G. & Bažant, Z., 1987. Nonlocal damage theory. *Journal of Engineering Mechanics*, vol. 113, n. 10, pp. 1512–1533.
- [7] de Borst, R. & Mühlhaus, H.-B., 1992. Gradient dependent plasticity: formulation and algorithmic aspects. *International Journal for Numerical Methods in Engineering*, vol. 35, pp. 521–539.
- [8] Peerlings, R., de Borst, R., Brekelmans, W., & de Vree, J., 1996. Gradient enhanced damage for quasi-brittle materials. *International Journal for Numerical Methods in Engineering*, vol. 39, pp. 3391–3403.
- [9] Peerlings, R., Geers, M., de Borst, R., & Brekelmans, W., 2001. A critical comparison of nonlocal and gradient-enhanced softening continua. *International Journal of Solids and Structures*, vol. 38, pp. 7723–7746.
- [10] Badnava, H., Mashayekhi, M., & Kadkhodaei, M., 2016. An anisotropic gradient damage model based on microplane theory. *International Journal of Damage Mechanics*, vol. 25, n. 3, pp. 336–357.
- [11] Needleman, A., 1988. Material rate dependence and mesh sensitivity in localization problems. *Computer Methods in Applied Mechanics and Engineering*, vol. 67, pp. 69–85.
- [12] Dugdale, D., 1960. Yielding of steel sheets containing slits. *Journal of the Mechanics and Physics of Solids*, vol. 8, pp. 100–104.
- [13] Barenblatt, G., 1962. The mathematical theory of equilibrium of crack in brittle fracture. *Advances in Applied Mechanics*, vol. 7, pp. 55–129.
- [14] Bažant, Z. & Oh, B., 1983. Crack band for fracture of concrete. *Matériaux et Constructions*, vol. 16, pp. 155–177.
- [15] Frémond, M. & Nedjar, B., 1996. Damage, gradient of damage and principle of virtual power. *International Journal of Solids and Structures*, vol. 33, n. 8, pp. 1083–1103.

- [16] Miehe, C., Welschinger, F., & Hofacker, M., 2010. Thermodynamically consistent phase-field models of fracture: Variational principles and multi-field FE implementations. *International Journal for Numerical Methods in Engineering*, vol. 83, pp. 1273–1311.
- [17] Miehe, C., Teichtmeister, S., & Aldakheel, F., 2016. Phase-field modelling of ductile fracture: a variational gradient-extended plasticity-damage theory and its micromorphic regularization. *Philosophical Transactions of the Royal Society A: Mathematical, Physical and Engineering Sciences*, vol. 374, n. 2066.
- [18] de Borst, R., 1991. Simulation of strain localization: a reappraisal of the Cosserat continuum. *Engineering Computations*, vol. 8, pp. 317–332.
- [19] de Borst, R. & Sluys, L., 1991. Localization in a Cosserat continuum under static and dynamic loading conditions. *Computer Methods in Applied Mechanics and Engineering*, vol. 90, pp. 805–827.
- [20] Sluys, L., 1992. *Wave propagation, localization and dispersion in softening solids*. PhD thesis, Technische Universiteit Delft, Delft, The Netherlands.
- [21] Dietsche, A., Steinmann, P., & Willam, K., 1993. Micropolar elastoplasticity and its role in localization. *International Journal of Plasticity*, vol. 9, pp. 813–831.
- [22] Iordache, M. & Willam, K., 1998. Localized failure analysis in elastoplastic Cosserat continua. *Computer Methods in Applied Mechanics and Engineering*, vol. 151, pp. 559–586.
- [23] Xotta, G., Bezaee, S., & Willam, K., 2016. Bifurcation investigation of coupled damage-plasticity models for concrete materials. *Computer Methods in Applied Mechanics and Engineering*, vol. 298, pp. 428–452.
- [24] Gori, L., Penna, S., & Pitangueira, R., 2017a. Discontinuous failure in micropolar elastic-degrading models. *International Journal of Damage Mechanics*, vol. 27, n. 10, pp. 1482–1515.
- [25] Gori, L., Penna, S., & Pitangueira, R., 2017b. An enhanced tensorial formulation for elastic degradation in micropolar continua. *Applied Mathematical Modelling*, vol. 41, pp. 299–315.
- [26] Gori, L., 2018. *Failure analysis of quasi-brittle media using the micropolar continuum theory, elastic-degrading constitutive models, and smoothed point interpolation methods*. PhD thesis, Universidade Federal de Minas Gerais (UFMG).
- [27] Ortiz, M., Leroy, Y., & Needleman, A., 1987. A finite element method for localized failure analysis. *Computer Methods in Applied Mechanics and Engineering*, vol. 61, n. 2, pp. 189–214.
- [28] Pietruszczak, S. & Mróz, Z., 1981. Finite element analysis of deformation of strain-softening materials. *International Journal for Numerical Methods in Engineering*, vol. 17, pp. 327–334.
- [29] Belytschko, T., Fish, J., & Engelmann, B., 1988. A finite element with embedded localization zones. *Computer Methods in Applied Mechanics and Engineering*, vol. 70, pp. 59–89.
- [30] Liu, W., Hao, S., Belytschko, T., Li, S., & Chang, C., 1999. Multiple scale meshfree methods for damage fracture and localization. *Computational Materials Science*, vol. 16, pp. 197–205.
- [31] Chen, J., Wu, T., & Belytschko, T., 2000. Regularization of material instabilities by meshfree approximations with intrinsic length scales. *International Journal for Numerical Methods in Engineering*, vol. 47, pp. 1303–1322.
- [32] Li, S., Hao, W., & Liu, W., 2000a. Mesh-free simulations of shear banding in large deformation. *International Journal of Solids and Structures*, vol. 37, pp. 7185–7206.
- [33] Li, S., Hao, W., & Liu, W., 2000b. Numerical simulations of large deformation of thin shell structures using meshfree methods. *Computational Mechanics*, vol. 25, pp. 102–116.

- [34] Chen, J., Zhang, X., & Belytschko, T., 2004. An implicit gradient model by a reproducing kernel strain regularization in strain localization problems. *Computer Methods in Applied Mechanics and Engineering*, vol. 193, pp. 2827–2844.
- [35] Chen, J., Hu, W., Puso, M., Wu, Y., & Zhang, X., 2007. Strain Smoothing for Stabilization and Regularization of Galerkin Meshfree Methods. In *Meshfree Methods for Partial Differential Equations III*, pp. 57–75. Springer Berlin Heidelberg, Berlin, Heidelberg.
- [36] Wang, D. & Li, Z., 2012. A two-level strain smoothing regularized meshfree approach with stabilized conforming nodal integration for elastic damage analysis. *International Journal of Damage Mechanics*, vol. 22, n. 3, pp. 440–459.
- [37] Gori, L., Penna, S., & Pitangueira, R., 2019a. Smoothed point interpolation methods for the regularization of material instabilities in scalar damage models. *International Journal for Numerical Methods in Engineering*, vol. 117, pp. 729–755.
- [38] Liu, G., 2009. *Meshfree Methods: Moving Beyond the Finite Element Method*. CRC Press - Taylor & Francis Group, New York, USA.
- [39] Liu, G., 2010a. A G space theory and a weakened weak (W^2) form for a unified formulation of compatible and incompatible methods: Part I theory. *International Journal for Numerical Methods in Engineering*, vol. 81, pp. 1093–1126.
- [40] Liu, G., 2010b. A G space theory and a weakened weak (W^2) form for a unified formulation of compatible and incompatible methods: Part II applications to solid mechanics problems. *International Journal for Numerical Methods in Engineering*, vol. 81, pp. 1127–1156.
- [41] Liu, G. & Zhang, G., 2013. *Smoothed Point Interpolation Methods - G Space Theory and Weakened Weak Forms*. World Scientific.
- [42] Gori, L., Penna, S., & Pitangueira, R., 2019b. G-space theory and weakened-weak form for micropolar media: Application to smoothed point interpolation methods. *Engineering Analysis with Boundary Elements*, vol. 101, pp. 318–329.
- [43] Geuzaine, C. & Remacle, J.-F., 2009. Gmsh: a 3D finite element mesh generator with built-in pre- and post-processing facilities. *International Journal for Numerical Methods in Engineering*, vol. 79, n. 11, pp. 1309–1331.
- [44] Eremeyev, V., 2005. Acceleration waves in micropolar elastic media. *Doklady Physics*, vol. 50, n. 4, pp. 204–206.
- [45] Mazars, J., 1984. *Application de la Mécanique de l'endommagement au comportement non linéaire et à la rupture du béton de Structure*. PhD thesis, Université Pierre et Marie Curie - Laboratoire de Mécanique et Technologie, Paris, France. (in french).
- [46] de Borst, R. & Gutiérrez, M. A., 1999. A unified framework for concrete damage and fracture models including size effects. *International Journal of Fracture*, vol. 95, n. 1-4, pp. 261–277.
- [47] Liu, G. & Gu, Y., 2001. A point interpolation method for two-dimensional solids. *International Journal for Numerical Methods in Engineering*, vol. 50, pp. 937–951.
- [48] Wang, J. & Liu, G., 2002. A point interpolation meshless method based on radial basis functions. *International Journal for Numerical Methods in Engineering*, vol. 54, pp. 1623–1648.
- [49] Liu, G., Zhang, G., & Dai, K., 2005. A linearly conforming point interpolation method (LC-PIM) for 2D solid mechanics problems. *International Journal of Computational Methods*, vol. 2, n. 4, pp. 645–665.

- [50] Liu, G. & Zhang, G., 2007. Upper bound solution to elasticity problems: a unique property of the linearly conforming point interpolation method (LC-PIM). *International Journal for Numerical Methods in Engineering*, vol. 74, pp. 1128–1161.
- [51] Zhang, G., Liu, G., Wang, Y., Huang, H., Zhong, Z., Li, G., & Han, X., 2007. A linearly conforming point interpolation method (LC-PIM) for three-dimensional elasticity problems. *International Journal for Numerical Methods in Engineering*, vol. 72, pp. 1524–1543.
- [52] Liu, G. & Zhang, G., 2008. Edge-based smoothed point interpolation methods. *International Journal of Computational Methods*, vol. 5, n. 4, pp. 621–646.
- [53] Winkler, B., Hofstetter, G., & Lehar, H., 2004. Application of a constitutive model for concrete to the analysis of a precast segmental tunnel lining. *International Journal for Numerical and Analytical Methods in Geomechanics*, vol. 28, pp. 797–819.
- [54] Arrea, M. & Ingraffea, A. R., 1982. Mixed mode crack propagation in mortar and concrete. Technical report, Department of Structural Engineering, Cornell University, Ithaca, USA.
- [55] Oliver, J., Huespe, a. E., Pulido, M. D. G., & Chaves, E., 2002. From continuum mechanics to fracture mechanics: The strong discontinuity approach. *Engineering Fracture Mechanics*, vol. 69, pp. 113–136.
- [56] Rabczuk, T. & Belytschko, T., 2004. Cracking particles: a simplified meshfree method for arbitrary evolving cracks. *International Journal for Numerical Methods in Engineering*, vol. 61, pp. 2316–2343.
- [57] de Borst, R., Gutiérrez, M. a., Wells, G. N., Remmers, J. J. C., & Askes, H., 2004. Cohesive-zone models, higher-order continuum theories and reliability methods for computational failure analysis. *International Journal for Numerical Methods in Engineering*, vol. 60, pp. 289–315.
- [58] Rabczuk, T. & Belytschko, T., 2007. A three-dimensional large deformation meshfree method for arbitrary evolving cracks. *Computer Methods in Applied Mechanics and Engineering*, vol. 196, pp. 2777–2799.
- [59] Jirásek, M., 2007. Nonlocal damage mechanics. *Revue Européenne de Génie Civil*, vol. 11, n. 7-8, pp. 993–1021.
- [60] Fang, X.-J., Jin, F., & Yang, Q.-D., 2008. Extended finite-element analysis of fractures in concrete. *Engineering and Computational Mechanics*, vol. 161, n. EM4, pp. 187–197.
- [61] Matallah, M. & La Borderie, C., 2009. Inelasticity-damage-based model for numerical modeling of concrete cracking. *Engineering Fracture Mechanics*, vol. 76, pp. 1087–1108.
- [62] Rajagopal, S. & Gupta, N., 2011. Meshfree modelling of fracture — A comparative study of different methods. *Meccanica*, vol. 46, pp. 1145–1158.
- [63] Ghosh, A. & Chaudhuri, P., 2013. Computational modeling of fracture in concrete using a meshfree meso-macro-multiscale method. *Computational Materials Science*, vol. 69, pp. 204–215.
- [64] Chaudhuri, P., 2013. Multi-scale modeling of fracture in concrete composites. *Composites Part B: Engineering*, vol. 47, pp. 162–172.
- [65] Yang, Y.-B. & Shieh, M.-S., 1990. Solution method for nonlinear problems with multiple critical points. *AIAA Journal*, vol. 28, n. 12, pp. 2110–2116.